Modeling lightning observations from space-based platforms (CloudScat.jl 1.0)

Alejandro Luque[1], Francisco José Gordillo-Vázquez[1], Dongshuai Li[1], Alejandro Malagón-Romero[1], Francisco Javier Pérez-Invernón[2], Anthony Schmalzried[1], Sergio Soler[1], Olivier Chanrion[3], Matthias Heumesser[3], Torsten Neubert[3], Víctor Reglero[4], and Nikolai Østgaard[5]

[1]Instituto de Astrofísica de Andalucía (IAA, CSIC), Granada (Spain)
[2]Institut für Physik der Atmosphäre, Deutsches Zentrum für Luft- und Raumfahrt, Wessling (Germany)
[3]National Space Institute, Technical University of Denmark (DTU Space), Kongens Lyngby (Denmark)
[4]Image Processing Laboratory, University of Valencia, Valencia (Spain)
[5]Birkeland Centre for Space Science, Department of Physics and Technology, University of Bergen, Bergen (Norway)

Correspondence: Alejandro Luque (aluque@iaa.es)

Abstract. We describe a computer code that simulates how a satellite observes optical radiation emitted by a lightning flash after it is scattered within an intervening cloud. Our code, CloudScat.jl, is flexible, fully open source and specifically tailored to modern instruments such as the Modular Multispectral Imaging Array (MMIA) component of the Atmosphere-Space Interactions Monitor (ASIM) that operates from the International Space Station. In this article we describe the algorithms implemented
5 in the code and discuss several applications and examples, with an emphasis on the interpretation of MMIA data.

1 Introduction

Lightning flashes emit intense optical radiation that, after passing through the cloud layer, can be observed from space. This has been applied to characterize the geographic and seasonal distributions of lightning (Christian et al., 2003; Cecil et al., 2014), to describe and forecast the development of particular thunderstorms (Peterson, 2019) and to investigate phenomena related to

10 lightning such as Transient Luminous Events (TLEs) (Ebert et al., 2010; Pasko et al., 2012) and Terrestrial Gamma-ray Flashes (TGFs) (Dwyer et al., 2012; Neubert et al., 2020).

Several satellite-borne instruments targeting lightning optical emissions have been commissioned in the past years and new ones are planned for the near future. The first such device was the Optical Transient Detector (OTD) (Christian et al., 2003), which was active from 1995 to 2000 onboard the Microlab-1 satellite. The OTD was a model for the longer-lasting Lightning

15 Imaging Sensor (LIS) that operated from the Tropical Rainfall Measurement Mission (TRMM) satellite from 1997 to 2015 (Boccippio et al., 2002; Mach et al., 2007; Zhang et al., 2019; Blakeslee, 2019). A second, identical LIS device has been installed in the International Space Station (ISS) since 2017 (Blakeslee et al., 2016).

After the success of space-based lightning observations from OTD and LIS, it became desirable, for operational weather prediction, to access real-time lightning data within a large geographic area. This was achieved by the Geostationary Lightning

20 Mapper (GLM) instruments onboard the Geostationary Operational Environmental Satellites (GOES) GOES-East and GOES-West (Goodman et al., 2013) and the Lightning Mapping Imager (LMI) on the Feng-Yun (FY-4) satellites. Also the Meteosat

Third Generation (MTG) constellation of satellites will be equipped with lightning-dedicated instruments named Lightning Imagers (LI).

All these instruments focus only on the detection of lightning flashes and they rely on cameras with wavelength filters centered around 777.4 nm, which is a strong emission line of lightning. Their integration times are around two milliseconds and their pixel sizes cover a few kilometers on the ground.

Other instruments target not only lightning but also additional phenomena associated with lightning. The Imager of Sprite/Upper Atmospheric Lightning (ISUAL) payload on the FORMOSAT-2 satellite contained limb-pointing cameras, spectrophotometers and a photometer array designed for the observation of TLEs between the cloud tops and the lower ionosphere (Chern et al., 2003). Although not its main focus, ISUAL detected routinely optical emissions from lightning. The Global Lightning and sprIte MeasurementS (GLIMS) mission, installed in the ISS, was equipped with imagers and photometers to observe lightning and TLEs towards the nadir (Sato et al., 2011; Adachi et al., 2016).

Our work is mainly motivated by another instrument that also has TLEs among its science objectives: the Modular Multispectral Imaging Array (MMIA), which is part of the Atmosphere-Space Interactions Monitor (ASIM) currently onboard the ISS (Chanrion et al., 2019; Neubert et al., 2020). Pointing towards the nadir of the ISS, MMIA is composed by two cameras and three photometers. The cameras provide images filtered around 777.4 nm and 337 nm, the latter wavelength being characteristic of non-thermal discharges that often accompany lightning flashes or are part of them. The camera pixels have a footprint on the ground of around $400\,\mathrm{m} \times 400\,\mathrm{m}$ at nadir and an integration time of 83.3 ms (yielding 12 frames per second). Of the three photometers, two are sensitive to the same wavelengths as the cameras whereas a third one detects an ultraviolet band approximately in the range 180-230 nm. The photometers operate at 10^5 samples per second. The high spatial resolution of MMIA's cameras and the high temporal resolution of its photometers enable detailed observations of lightning flashes that are nevertheless conditioned by scattering within the intervening clouds. This is why this instrument demands an improved understanding of this scattering.

In order to interpret the observations of these instruments one must understand how the optical radiation emitted by a lightning flash is scattered inside a cloud, sometimes with an intricate shape. For example, the strong convection generally associated with active thunderclouds causes overshooting cloud turrets and light emerging from them is partially reflected back upwards from the lower cloud deck, as illustrated by Chanrion et al. (2017). Because the optical properties of a lightning flash as observed from above are conditioned by the properties of the cloud where it originated, they may serve to characterize thunderstorms, as recently proposed by Peterson (2019) and also to investigate the time structure of lightning discharges (Peterson and Rudlosky, 2019).

Quantitative models of optical lightning radiation passing through clouds were developed in the past by e.g. Thomason and Krider (1982), Koshak et al. (1994) and Light et al. (2001) but they were limited to relatively simple cloud geometries and considered only how the radiation is delayed, disregarding image composition.

Here we present CloudScat.jl, a code that overcomes these two limitations and serves as an open-source tool for the interpretation of space-based lightning observations. CloudScat.jl deals efficiently with complex cloud shapes defined by the

composition of elemental solids such as spheres, cylinders and cones that can be arbitrarily placed and deformed. It also predicts the images recorded from observing devices located anywhere relative to the lightning source.

2 Model and numerical algorithm

Our algorithm is partly based on those described by Thomason and Krider (1982) and Light et al. (2001) but extended with
60 additional physical processes and variance-reducing methods. It simulates the propagation of a set of photon packets that interact with a background that includes both cloud hydrometeors and the molecular components of air. Since the types of processes that we consider do not change the photon's wavelength, in each simulation we consider only a monochromatic population of photons with a certain wavelength λ. Roughly our model is applicable for wavelengths from around 200 nm to 1 μm.

65 Every photon packet propagates asynchronously and independently of all other packet, so in what follows we describe the dynamics of a single packet. We will also sometimes write *photon* as a shortcut for a computational particle, which properly should be considered as an ensemble of physical photons. Each of these photon packets or computational particles is assigned a statistical weight to account for the different number of physical particles that it represents.

We consider two types of proccess. Scattering proccesses that modify the propagation direction of the photons are modelled
70 as a series of discrete, stochastic events. Molecular absorption is treated as a continuous process that dampens the statistical weight of the packet as it propagates.

Regarding the discrete scattering events, our notation is that the ith collision takes place at location $\boldsymbol{r}_i$ and time t_i (see figure 1). Immediately before the collision the photon weight is w_i^- and its velocity is $c\boldsymbol{\mu}_{i-1}$ with c being the speed of light and $\boldsymbol{\mu}_{i-1}$ a unitary vector. The collision instantaneously changes these magnitudes to w_i^+, $c\boldsymbol{\mu}_i$. Due to background absorption,
75 the weight decays through the propagation path of a photon so $w_{i+1}^- \leq w_i^+$, with equality holding in the absence of absorption. All photons are initialized at $t_0 = 0$ with weight $w_0^+ = 1$, random locations $\boldsymbol{r}_0$ uniformly distributed in one straight segment and an isotropic distribution of $\boldsymbol{\mu}_0$. All our output results are divided by the number of initial photons N, so intensities must be interpreted as intensity per physical photon in the source (equivalently we could initiatialize all weights to $1/N$ but this would complicate our description).

80 As a photon advances, it collides with background scatterers at a total rate per unit time

$$\nu(\boldsymbol{r}) = c \sum_{p=1}^{m} \bar{\sigma}_p(\boldsymbol{r}) n_p(\boldsymbol{r}), \tag{1}$$

where c is the speed of light, $\bar{\sigma}_p(\boldsymbol{r})$ is the locally-averaged cross section and $n_p(\boldsymbol{r})$ the number density of the scatterers involved in the process p at location $\boldsymbol{r}$. The cross sections are averaged locally because around a given point there may exist a full spectrum of scattering particles with different cross sections (due to, for example, different radii of cloud droplets). To sample
85 the interaction times we employ the null collision method, whereby we find one rate ν_T such that $\nu_T > \nu(\boldsymbol{r})$ everywhere inside the computational domain. The time of the ith scattering, including null collisions, is

$$t_i = t_{i-1} - \nu_T^{-1} \log(\xi_{i-1}), \tag{2}$$
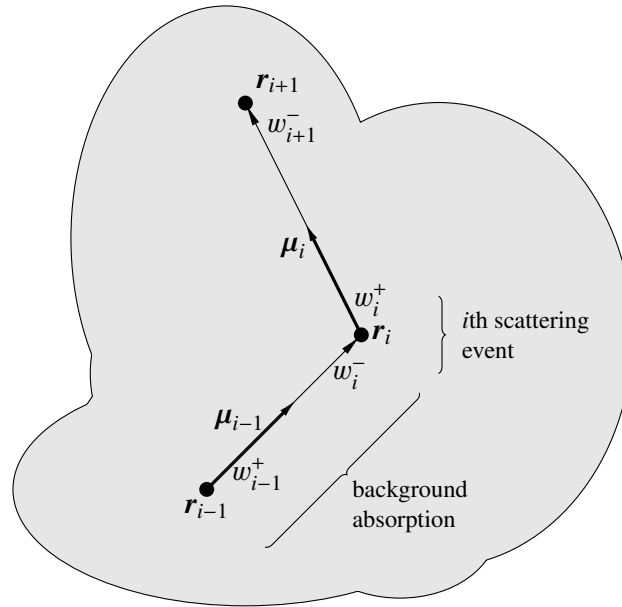
Figure 1. Sketch with the notation employed in this work. We account for two types of processes affecting photon propagation. Mie and Rayleigh scattering are modelled as discrete scattering events that take place at locations $r_1, \ldots, r_{i-1}, r_i, r_{i+1}, \ldots$. Because Mie scattering dissipates part of the photon's energy, in the ith scattering event the particle's statistical weight changes from w_i^- to w_i^+. The absorption by background molecular components of air modifies the particle statistical weight as it propagates between consecutive scattering events. This changes the particle's weight e.g. from w_{i-1}^+ immediately after scattering $i-1$ to w_i^- immediately before scattering i.

where the ξ_i are independent random variables uniformly distributed in the interval $[0,1]$. The type of interaction is decided with probabilities allotted proportionally to each individual rate and with probablity $1 - \nu(r)/\nu_T$ for a null collision.

2.1 Mie scattering

In Mie scattering a photon packet with a wavelength λ interacts with a cloud droplet, modeled as a dielectric sphere with a radius $R \gg \lambda$ (van de Hulst, 1981). The cross section of this interaction is

$$\sigma_{\text{Mie}} = Q_{\text{ext}}(R)\pi R^2, \tag{3}$$

where Q_{ext} is called *extinction efficiency* and is generally close to two (the fact that this is not one, as the naive application of geometrical optics would suggest, is called *extinction paradox* and is discussed at length in e.g. (Bohren and Huffman, 1983, p. 107)). The incident radiation is partially absorbed by the droplet, letting a fraction ω_0 (called *single-scattering albedo*) of the energy being re-emitted. In our code we account for this absorption by updating the weight w_i^- as follows. First we compute a temporary weight w_i' as

$$w_i' = \omega_0 w_i^-. \tag{4}$$

100   If w'_i is larger than a prescribed $w_{min} < 1$ we set $w^+_i = w'_i$. Otherwise we set $w^+_i = 1$ with probability w'_i and $w^+_i = 0$ with probability $1 - w'_i$ (i.e. in the second case we discard the photon). We thus avoid computations on photons with so little weight that they do not affect the observations but ensure that the expected value of w^+_i is w'_i and we are not biasing the simulation (Iwabuchi, 2006). The default value of w_{min} is 10^{-2}.

The outgoing electromagnetic wave after Mie scattering is sampled by deflecting the direction of the incident photon. The

105   scattered intensity per unit solid angle at a given direction forming an angle θ with the incident direction is conventionally named *phase function* and here, following Thomason and Krider (1982) we approximate it by the Henyey-Greenstein phase function,

$$p_{HG}(\theta) = \frac{1 - g^2}{(1 + g^2 - 2g\cos\theta)^{3/2}}. \tag{5}$$

By convention any phase function $p(\theta)$ is normalized such that

110   $$\int_0^\pi p(\theta)\sin(\theta)\,d\theta = 4\pi. \tag{6}$$

The Henyey-Greenstein phase function is parametrized by g, called *asymmetry parameter* which is the average of the cosine of the scattering angle,

$$g = \frac{1}{4\pi}\int_0^\pi p(\theta)\cos(\theta)\sin(\theta)\,d\theta. \tag{7}$$

Given an arbitrary phase function obtained, for example, by an accurate solution of the Mie scattering problem one can compute

115   an assymetry parameter through (7) and then approximate the accurate phase function by the Henyey-Greenstein function with the same g. One advantage of this is that it is simple and efficient to sample the Henyey-Greenstein phase function by inverting the cumulative probability distribution of $\cos\theta$. The result is that one can draw a random number s uniformly distributed between -1 and 1 and then set

$$\cos\theta = \frac{1}{2g}\left[1 + g^2 - \left(\frac{1 - g^2}{1 + gs}\right)^2\right]. \tag{8}$$

120   To compute the three parameters of Mie scattering, Q_{ext}, ω_0 and g, which depend on the wavelength of interest and the droplet radius, we solve the Mie problem with the open source MieScatter.jl code (Wilkman, 2013). A required input for the Mie solver is the refractive index of the medium and the code allows the user to specify this from an input file. The uppermost layers of a thundercloud are above the glaciation line so the water content is predominantly in ice form. Nevertheless the optical constants of water and ice are rather similar, the main difference being that absorption in ice is negligible in the range of wavelengths

125   from 200 to 400 nm (Warren and Brandt, 2008) and therefore, for the sake of simplicity, here we mostly employ the water optical constants, which we interpolate from Hale and Querry (1973). In most cases reported here the difference between ice and water is rather small and only when studying far-ultraviolet radiation in section 3.2 will we consider ice clouds.

In general the droplet size spectrum of a convective cloud is inhomogeneous and assuming a constant radius everywhere may be an oversimplification. A somewhat more accurate model approximates the full spectrum of radii with a single, effective

radius R but allows it to depend on the scattering position. In that case the average cross-section as well as the phase function depend on the location of the scattering event. This can optionally be implemented in the code by using a parametrized dependence of the Mie scattering features as a function of R. After inspecting plots of accurate solutions and aiming for simplicity, we settled on these expressions to which we do not attribute any physical meaning:

$$Q_{\text{ext}}(R) = 2 + bR^{-3/4}, \tag{9a}$$

$$\omega_0(R) = 1 - aR, \tag{9b}$$

$$g(R) = \frac{g_0 R}{R + R_0}, \tag{9c}$$

where a, b, g_0 and R_0 are fitting parameters. These functions are simple but still capture the dependence of the scattering parameters on R. The user of our code can ask to solve the Mie scattering problem for a range of radius $1\,\mu\text{m} < R < 100\,\mu\text{m}$, fit the results to the above functions and use the result to build an inhomogeneous model for the cloud.

2.2 Rayleigh scattering

As optical radiation travels inside the cloud or in the path to a space platform it is also affected by interactions with the molecular components of air. For lightning emissions this is generally a negligible correction but we included them in our code for the sake of completeness and to eventually allow for additional applications.

To compute the Rayleigh scattering cross section we follow Bodhaine et al. (1999), which gives

$$\sigma_{\text{R}} = \frac{24\pi^3 F(\text{air})}{\lambda^4 N_0^2} \left(\frac{n_s^2 - 1}{n_s^2 + 2}\right)^2, \tag{10}$$

where N_0 is the number density of air at standard temperature and pressure (Loschmidt's constant), n_s is the refractive index of air under those conditions and $F(\text{air})$ is a so called *depolarization term* or King factor, which corrects the Rayleigh theoretical estimates to account for the asymmetry of scattering molecules. We compute n_s as suggested by Peck and Reeder (1972):

$$10^8(n_s - 1) = 8060.51 + \frac{2\,480\,990}{132.274 - \lambda^{-2}} + \frac{17\,455.7}{39.329\,57 - \lambda^{-2}}, \tag{11}$$

where λ is expressed in micrometers. We calculated $F(\text{air})$ from the formulas provided by Bates (1984), as also compiled by Bodhaine et al. (1999) with the air composition from (Haynes, 2016, p. 14-19).

The phase function for Rayleigh scattering is

$$p_{\text{R}}(\theta) = \frac{3}{4}(1 + \cos^2 \theta). \tag{12}$$

and after inverting the cumulative probability distribution of $\cos\theta$ can be sampled as

$$\cos\theta = w^{1/3} - w^{-1/3}, \; w = 2s + (4s^2 + 1)^{1/2}, \tag{13}$$

where s is a random number uniformly distributed in $[-1, 1)$.

The collision rate reads $\nu_R = cN(z)\sigma_R$, where $N(z)$ is the number density of air at a given altitude z. Because Rayleigh
160 scattering is a small correction on top of the much more relevant Mie scattering, we implemented a simple model where the air density decreases exponentially with altitude:

$$N(z) = N_0 \exp(-z/H), \tag{14}$$

where H is the scale height, which is user-configurable and defaults to $7.2\,\mathrm{km}$.

2.3 Background absorption

165 Some wavelengths of interest for the observation of lightning are significantly absorbed in air. For example, the band 180-230 nm probed by one of MMIA's photometer is affected by molecular absorption by ozone (Molina and Molina, 1986) and by the Schumann-Runge band of molecular oxygen (Minschwaner et al., 1992). Although in principle one could incorporate this into our code by an additional discrete process that randomly discards some of the computational particles, it is more efficient, in terms of a lower variance in the output for the same computational time, to continuously adapt the statistical weight of the
170 particles along their propagation.

For a single absorbing species, in the propagation between two collision points $\mathbf{r}_i$ and $\mathbf{r}_{i+1}$ the weight of the photon changes according to the Beer-Lambert law:

$$w_{i+1}^- = w_i^+ \exp\left(-\int_{\mathbf{r}_i}^{\mathbf{r}_{i+1}} \sigma_{abs} n_{abs}(\mathbf{r})\,dr\right), \tag{15}$$

where the integral is along the straight line between $\mathbf{r}_i$ and $\mathbf{r}_{i+1}$, σ_{abs} is the absorption cross section and n_{abs} is the number
175 density of the absorbing species.

In our code we implemented the most common case of a stratified atmosphere where n_{abs} depends only on the altitude z. In that case we can avoid computing the integral in (15) for every propagation step. This is implemented by computing during the code initialization a cumulative density

$$M(z) = \int_0^z n_{abs}(z')\,dz'. \tag{16}$$

180 This integral is computed within a grid of altitudes and then linearly interpolated for arbitrary z between the gridpoints. The integral in (15) can be rewritten as

$$\int_{\mathbf{r}_i}^{\mathbf{r}_{i+1}} \sigma_{abs} n_{abs}(\mathbf{r})\,dr = \frac{\sigma_{abs}|M(z_{i+1}) - M(z_i)|}{|\mu_i^z|}, \tag{17}$$
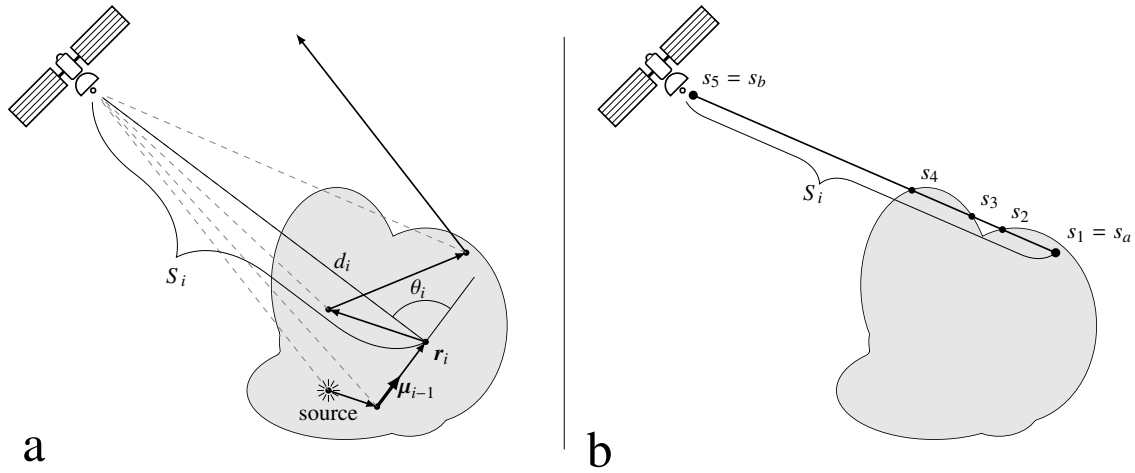
Figure 2. Ouline of the local estimation method. (a) For a given packet we add the contributions to the radiated energy reaching a detector from each scattering event. (b) These contributions are affected by the optical depth of the scattering location, which involves an integral from that point to the detector. The integral is divided into segments where the collision rate is smooth.

where μ_i^z is the z-component of the unitary vector pointing from $\boldsymbol{r}_i$ to $\boldsymbol{r}_{i+1}$ and we assumed $\mu_i^z \neq 0$. In the unlikely case that, within working precision, the photon propagation is horizontal we have

$$\int_{\boldsymbol{r}_i}^{\boldsymbol{r}_{i+1}} \sigma_{\mathrm{abs}} n_{\mathrm{abs}}(\boldsymbol{r})\, dr = \sigma_{\mathrm{abs}} n(z_i) |\boldsymbol{r}_{i+1} - \boldsymbol{r}_i|. \tag{18}$$

2.4 Local estimation method

Typically in our code we consider 10^6 to 10^7 photon packets and we simulate the signal received by an observer hundreds of kilometers away from the source. With these numbers the probability that a significant number of photons packets would emerge from the area covered by one image pixel and reach the detector is negligible. For this reason we cannot simulate an image by accounting only for the final, outgoing direction of the simulated photons. We overcome this problem by means of a local estimation method as described e.g. by Iwabuchi (2006). This method is sketched in figure 2a and may be understood as follows.

After the ith collision the energy of the photon packet is radiated in all directions according to the incident direction $\boldsymbol{\mu}_{i-1}$ and the phase function $p(\theta)$ (either p_{R} or p_{HG}). Consider a detector with a surface area A at a long distance from the scattering event d_i with $A \ll 4\pi d_i^2$. The energy that reaches this detector is

$$\delta_i = \frac{A w_i^- p(\theta_i)}{4\pi d_i^2} \exp(-\tau_i), \tag{19}$$

where the energy is normalized to that of a photon of the given wavelength with unitary weight, θ_i is the angle between $\boldsymbol{\mu}_{i-1}$ and the line of sight S_i of the event $\boldsymbol{r}_i$ and τ_i is the optical depth defined as

$$\tau_i = \int\limits_{S_i} \nu_{\text{all}}(s)\, ds, \tag{20}$$

200   where s is a coordinate indexing the line of sight S_i (with length d_i) and ν_{all} includes all processes that may affect a photon (Mie scattering, Rayleigh scattering and background absorption). During a simulation we bin all δ_i according to their direction of arrival to the detector to form an image or according to their arrival time $t'_i = t_i + d_i/c$ to simulate a photometer waveform. For this purpose, to set up a run the user must specify the features of one or several observing devices, including their location and the field-of-view and image size of their cameras and the frame rate of their photometers. In all photometer plots of this

205   paper our initial time is the time of arrival of an hypothetical unscattered source photon.

The components of τ_i stemming from Rayleigh scattering and background absorption are computed using an analytical expression for Rayleigh scattering and with the method described in the previous section for background absorption, trivially adapted for the propagation towards an observer.

However, for a general cloud geometry the integration path in (20) sometimes traverses several cloud boundaries (see fig-

210   ure 2b) where the Mie component of the collision rate (ν_{Mie}) presents discontinuities. We take this into account by dividing the path $S_i = (s_a, s_b)$ into n sub-intervals $(s_1 = s_a, s_2), \ldots, (s_n, s_{n+1} = s_b)$ and rewriting the integral as

$$\tau_{i,\text{Mie}} = \sum_{k=1}^{n} \int\limits_{s_k}^{s_{k+1}} \nu_{\text{Mie}}(s)\, ds, \tag{21}$$

where we can assume each integrand to be smooth. Each integral, from s_k to s_{k+1} is computed numerically via a Gauss-Legendre quadrature with an order that defaults to three but can be configured by the user.

215   The integrals in (21) are computationally expensive and take a significant portion of the computations. In some cases, however, they can be skipped: if a scattering event happens deep within the cloud, τ_i is so large that the contribution of δ_i is negligible. To account for this and save computational time the user can select a minimum altitude z_{min} below which (21) is not computed and the corresponding δ_i is set to zero.

Note that in the local estimation method a single photon packet leaves observation traces from more than a single time and

220   place and thus creates spureous correlations in the predicted observations. These correlations are visible when the simulated signal is weak but they do not pose a practical concern.

2.5 Cloud geometry

The CloudScat code admits arbitrarily complex cloud geometries. The user constructs the cloud shape by means of boolean combinations and affine transformations of elementary solid figures. The code is equipped with a library of figures including a

225   sphere, a cylinder, a cone and a half-space delimited by a plane. This can be extended with user-defined figures by implementing methods that (a) compute the intersections of the figure's boundary with a straight line and (b) determine whether the figure contains a given point.

The supported boolean operations are:

1. Union of several figures $F_1 \ldots F_M$: a point is contained in the union $\cup_{i=1}^{M} F_i$ if its contained in any F_i.

230   2. Intersection of several figures $F_1 \ldots F_M$: a point is contained in the intersection $\cap_{i=1}^{M} F_i$ if its contained in all F_i.

3. Difference of two figures F_1 and F_2: a point is contained in the difference $F_1 \setminus F_2$ if it is contained in F_1 but not in F_2.

These operations can be nested to an arbitrary depth, constructing for example the difference between an union and an intersection.

The figures (and any boolean combination thereof) may also be transformed by affine transformations $\mathcal{A}$ consisting of a

235   translation vector $\boldsymbol{R}$ and an invertible matrix $\mathbf{M}$. A point $\boldsymbol{r}$ belongs to the transformed figure $\mathcal{A}F$ if $\boldsymbol{r}' = \mathbf{M}^{-1}\boldsymbol{r} - \boldsymbol{R}$ belongs to F. This means linearly transforming the shape with $\mathbf{M}$ and afterwards translating it along $\boldsymbol{R}$. Again, affine transformations can be combined with other affine transformations and boolean operations up to an arbitrary depth.

3   Examples and applications

3.1   Photon diffusion model

240   In part as a verification of the code and in part as a modelling tool we first consider the heavily simplified case of a point-like lightning source inside a homogeneous, infinite cloud with a planar top that we set at $z = 0$. In this section we also neglect Rayleigh scattering and background absorption and set a homogeneous collision rate $\nu = cN_d Q_{\text{ext}}\pi R^2$, where N_d is a droplet number density and Q_{ext} and R are the extinction coefficient and droplet radius, also assumed to be homogeneous.

Koshak et al. (1994) applied classical methods of transport theory to the problem of radiation propagation inside a cloud.

245   By truncating the spherical-harmonic expansion of the one-speed Boltzmann equation, they showed that the photon density ψ approximately follows a diffusion equation with an absorption term:

$$\frac{\partial \psi}{\partial t} - \nabla \cdot (D\nabla\psi) = -\frac{\psi}{\tau_A}, \tag{22}$$

where the diffusion coefficient D is

$$D = \frac{c^2}{3\nu(1 - g\omega_0)}, \tag{23}$$

250   and

$$\tau_A = \frac{1}{\nu(1 - \omega_0)} \tag{24}$$

is the photon absorption time. Equation (22) must be supplemented by the condition $\psi(z = 0) = 0$ imposed by the perfectly absorbing boundary (photons at locations $z > 0$ never reach the cloud again).

The solution of (22) with the appropriate boundary condition and initial condition $\psi(\boldsymbol{r}, t = 0) = \delta(x)\delta(y)\delta(z-L)$ corresponding

255 to a point source at $(0, 0, -L)$ is found by the method of images (Krapivsky et al., 2010, p. 32) and reads

$$\psi(x,y,z) = \frac{e^{-t/\tau_A}}{(4\pi Dt)^{3/2}}\left[\exp\left(\frac{-x^2-y^2-(z+L)^2}{4Dt}\right) - \exp\left(\frac{-x^2-y^2-(z-L)^2}{4Dt}\right)\right]. \tag{25}$$

From this expression one obtains the instantaneous flux of photons emerging from the cloud at $(x, y, 0)$ and time t as

$$f(x,y,t) = D\left(\frac{\partial\psi}{\partial z}\right)_{z=0} = \frac{Le^{-t/\tau_A}}{(4\pi D)^{3/2}t^{5/2}}\exp\left(\frac{-x^2-y^2-L^2}{4Dt}\right). \tag{26}$$

And, integrating in the (x, y) plane this yields a total flux per unit time

260 $$F(t) = \int_{-\infty}^{\infty}dx\int_{-\infty}^{\infty}dy\,f(x,y,t) = \frac{e^{-t/\tau_A - \tau_D/t}}{\pi^{1/2}\tau_D}\left(\frac{t}{\tau_D}\right)^{-3/2}, \tag{27}$$

where we have introduced the characteristic time for the photons to diffuse up to a distance L,

$$\tau_D = \frac{L^2}{4D}. \tag{28}$$

On the other hand, integrating (26) in time gives an expression for the number of photons that exit the cloud from a given location at anytime,

265 $$\Phi(x,y) = \int_{0}^{\infty}dt\,f(x,y,t) = \frac{1}{2\pi(L^2+\rho^2)}\left(\frac{L}{(L^2+\rho^2)^{1/2}} + 2\epsilon\right)\exp\left(-\frac{2\epsilon(L^2+\rho^2)}{L}\right), \tag{29}$$

where we have introduced $\rho = (x^2+y^2)^{1/2}$ and $\epsilon = (\tau_D/\tau_A)^{1/2}$. In cases where the absorption of photons can be neglected (i.e. the time of absorption τ_A is much larger than the characteristic diffusion time τ_D) equation (29) reduces to

$$\Phi(\rho) = \frac{L}{2\pi(L^2+\rho^2)^{3/2}}, \tag{30}$$

which remarkably leads to a spatial distribution of optical radiation that does not depend on the Mie scattering parameters but
270 only on the source depth L.

Soler et al. (2020) fitted expression (27) to the MMIA photometer signal in order to infer the altitudes of presumed Fast Breakdown events (Rison et al., 2016) associated with radio-detected Narrow Bipolar Events (Le Vine, 1980; Smith et al., 1999; Liu et al., 2018). They obtained a best-fit τ_D and via (28), given a plausible bracket for D, derived an interval for L which, combined with independent measurements of the cloud-top-height provides a range of source altitudes.

275 Another approach to estimate the source depth is by means of the spatial distribution described by (30), which offers the advantage that it does not demand an assumed D. This is however limited to cases where absorption is weak and the irregularities of the cloud top do not affect too much the recorded image. Both these conditions generally imply that the source is not too deeply buried in the cloud.

Clearly, both of these approaches to estimate the source depth also depend on approximating the source as point-like. This is
280 acceptable for Fast Breakdown events which span some hundreds of meters (Rison et al., 2016; Tilles et al., 2019) but becomes more questionable for other types of events.
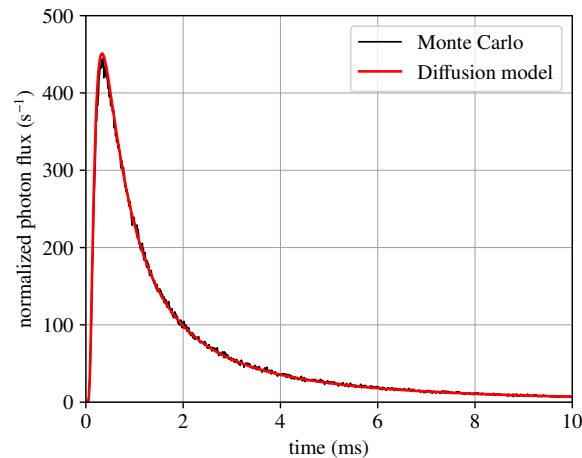
Figure 3. Total photon flux emerging from a semi-infinte cloud. The cloud extends infinitely below 15 km and the photon source is located at 10 km . We compare a Montecarlo (black) and a analytically-solvable diffusion model (red). The photon flux is normalized with respect to the number of source photons (i.e. must be interpreted as the flux per source photon). The parameters of the model curve are $\tau_D = 0.503\,\text{ms}$, $\tau_A = 18.5\,\text{ms}$. Here and in all subsequent photometer plots, the time origin corresponds to the arrival time of an unscattered photon.

Let us apply our Monte Carlo model to this configuration. We run the code for a point source within an infinite, homogeneous cloud. The cloud top is set at 15 km and the source at 10 km. The cloud is composed by droplets with radius $R = 10\,\mu\text{m}$ and a density $N_d = 100\,\text{cm}^{-3}$ and we consider the propagation of radiation with a wavelength $\lambda = 337\,\text{nm}$. The resulting Mie scattering parameters are $g = 0.874$, $\omega_0 = 1 - 2.82 \times 10^{-6}$, $Q_\text{ext} = 2 + 3.99 \times 10^{-2}$.

The photons emerging from the cloud have a slight preference for the direction perpendicular to the cloud boundary so the radiance is not perfectly Lambertian. To compare with the analytical expressions derived above we must integrate the emissions in all directions. Making use of the azymuthal symmetry of the emissions, we achieve this by setting several observers, all of them at a distance of 400 km from the point in the cloud top closest to the source but varying the zenith angle of observation. We chose these angles to perform a 5-point Gauss-Legendre quadrature of the photon flux in all directions. Figure 3 compares the Montecarlo results and expression (27). We consider the agreement of the two curves as a verification of the code implementation as well as of the diffusion model proposed by Koshak et al. (1994).

Our next step is to take into account that the cloud is not infinitely deep and therefore some photons exit through the lower boundary. We consider now a cloud limited by two infinite parallel planes. The method of images is also suitable for this problem but the solution is composed by an infinite sum of contributions from virtual images arranged in a periodic lattice. Assume that the cloud extends from $z = 0$ to $z = -b$ and the photon source is again at $z = -L$. The resulting lattice consists of positive images at $z \in \{-L + 2bn : n \in \mathbb{Z}\}$ and negative images at $z \in \{L + 2bn : n \in \mathbb{Z}\}$. The contribution of each image to the

integrated flux of photons at $z = 0$ reads

$$F_n^\pm(t) = \pm \frac{2\pi D e^{-t/\tau_A}}{(4\pi Dt)^{3/2}}(\mp L + 2bn)\exp\left(-\frac{(\mp L + 2bn)^2}{4Dt}\right).$$ (31)

300 Noting that $F_n^\pm = F_{-n}^\mp$ we write the total flux as

$$F(t) = \frac{4\pi D e^{-t/\tau_A}}{(4\pi Dt)^{3/2}}\sum_{n\in\mathbb{Z}}(L + 2bn)\exp\left(-\frac{(L + 2bn)^2}{4Dt}\right).$$ (32)

Notice that if we keep only the $n = 0$ term in this series we recover expression (27). For long times, the series (32) requires the unwieldy addition of a large number of terms. Therefore to obtain the long-time behaviour of $F(t)$ we use the following identity that results from Poisson's summation formula and is valid for arbitrary u, v:

305 $$\sum_{n\in\mathbb{Z}}(u + nv)e^{-(u+nv)^2} = \frac{2\pi^{3/2}}{v^2}\sum_{k=1}^{\infty}k\sin\left(\frac{2\pi ku}{v}\right)e^{-\frac{\pi^2 k^2}{v^2}}.$$ (33)

This allows us to cast formula (32) into

$$F(t) = \frac{2\pi D e^{-t/\tau_A}}{b^2}\sum_{k=1}^{\infty}k\sin\left(\frac{\pi k L}{b}\right)\exp\left(-\frac{\pi^2 k^2 Dt}{b^2}\right),$$ (34)

which for long t converges faster than (32). Indeed, from the slowest-decaying term $k = 1$ we extract a decay time

$$\tau_S = \frac{b^2}{\pi^2 D}.$$ (35)

310   To check our code against these expressions we run a simulation with the same microscopical parameters as used above for figure 3 but in this case the cloud exists only above 7 km altitude. The photon source is again at 10 km and thus closer to the lower boundary than to the cloud top. In this situation we expect (27) to perform poorly for long times. This is indeed the case as we show in figure 4, where we plot the Monte Carlo results together with expression (27), which disregards the lower boundary, and also two truncations of the series (34) that keep one and two terms. We see that the long term behaviour

315 is perfectly captured by the $k = 1$ term in the series. At early times the approximation is much improved by including a second term of the sum. For small t equation (27) is closer to the simulation curve; this is because that expression is a one-term truncation of the series (32), wich converges faster as $t \to 0$.

3.2 Ozone absorption

As we mentioned above, the absorption of radiation by the molecular components of air cannot be neglected for certain

320 wavelengths. A case in point is the absorption by ozone of the far-ultraviolet radiation in the range 180-230 nm, to which one of the MMIA photometers is sensitive. This photometer was conceived for light emanating from TLEs in the upper atmosphere (Neubert et al., 2020) but it may also be sensitive to lightning emissions. Here we investigate this possibility by simulating the photometer response to a far-ultraviolet source inside a thundercloud.

    We selected a wavelength of 200 nm, where the absorption cross-section of ozone reaches a minumum $\sigma_{abs} = 3.145 \times$

325 10^{-19} cm^2 (Molina and Molina, 1986). This is therefore the best-transmitted wavelength, although we do not know if strong emission lines are present around this wavelength in a lightning flash.
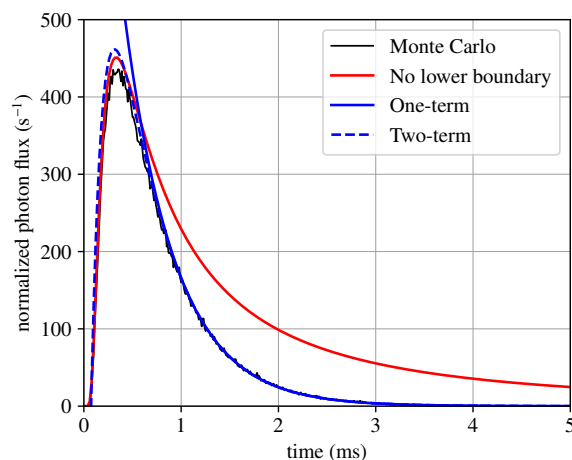
Figure 4. Total photon flux emerging from the top of a planar homogeneous 8 km-thick cloud. We plot the Monte Carlo simulation results (black) together with analytical expression for a cloud without the lower bound (red; same as figure 3) and the one and two-term truncations of the analytical approximation (blue; see text). Note that the two-term approximation reaches unphysical negative values for small time although this is barely discernible in the plot.

The ozone density inside a thunderstorm is also uncertain and may differ significantly from a fair-weather density because it is affected by the strong convection and electrical activity of the thunderstorm (Pan et al., 2014; Bozem et al., 2014). Nevertheless, for illustration purposes, we selected several profiles of ozone in the atmosphere corresponding to those implemented
330 in the MODTRAN 5 code (Berk et al., 2005) as previously introduced by Kneizys et al. (1980) for the LOWTRAN code. They correspond to Tropical (15°N), Midlatitude Summer (45°N, July) and Midlatitude Winter (45°N, January) conditions as well as to the U.S. Standard Atmosphere (United States Committee on Extension to the Standard Atmosphere, 1976). We disregard Subarctic conditions as they are not relevant for lightning. The ozone profiles are displayed in the left panel of figure 5.

We implemented these ozone profiles in simulations with the same cloud configuration as in the previous section (10-μm-
335 droplets with a density of $100\,\text{cm}^{-3}$ in a cloud spanning from 7 to 12 km; source at 10 km) but with a 200-nm source. Besides the role of molecular absorption, this wavelength also underlines differences between the absorption properties of water and ice: whereas water absorbs 200-nm radiation strongly, absorption by ice is negligible. However we observe this difference only when molecular absorption by ozone does not dominate. The Tropical case, for example, has the lowest ozone density and thus allows us to see different absorption rates between water and ice. Therefore for that ozone profile we run simulations using
340 both ice and water optical constants. Note also that now we are not interested in the total photon flux emerging from the cloud top so we simulated the response of a single photometer located at an altitude of 400 km directly above the source.

The results, plotted in the right panel of figure 5 show the signal decaying quickly within a fraction of a millisecond. If the ozone density (n_{O3}) was homogeneous within the cloud the decay time would be

$$\tau_{O3} = c\sigma_{\text{abs}}n_{O3}. \tag{36}$$
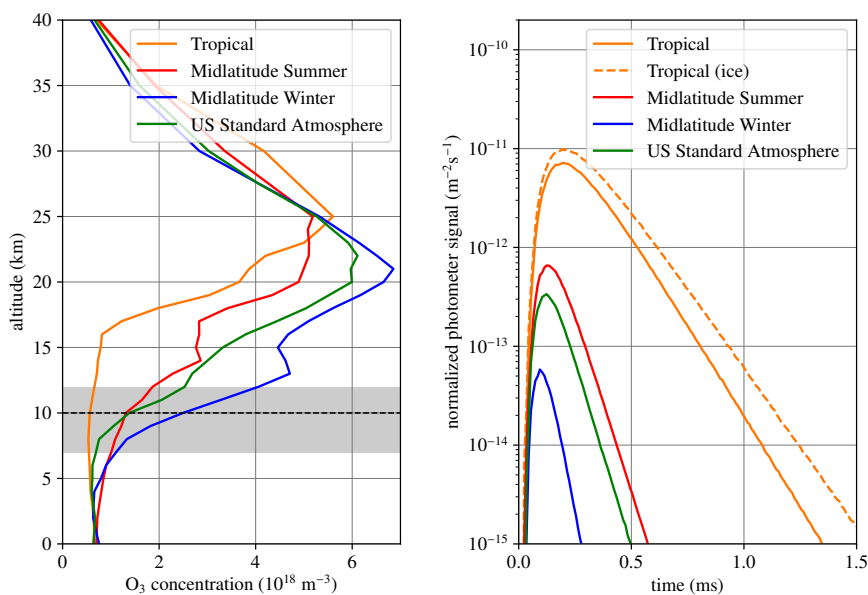
Figure 5. The role of ozone absorption in the photometer signal from a lightning flash. The left panel shows several ozone profiles employed in Monte Carlo simulations. The shaded area marks the extent of the cloud and the horizontal dashed line the location of the source. In the right panel we show the simulated photometer response to a 200-nm source observed from above at an altitude of 400 km. Excepting the indicated case, all simulations use the water refractive index. The shaded areas indicate the range of exponential decay rates corresponding to the ozone density at the location of the source and at the cloud top (bear in mind that only the slopes of these curves are relevant: they are placed to pass through the peak of the Monte Carlo curves).

345   However, with the selected profiles, the photons explore regions with markedly different ozone densities. In the left panel of figure 5 we indicate, by means of a shaded region, the range of decay rates between the source location (slowest decay) and the cloud top (the fastest decay). In most cases the decay rate is between the two extreme values predicted by the ozone concentrations at the source and at the cloud top. The exception is the Tropical ozone profile, where the strong absorption by water droplets leads to a somewhat faster decay. If we use the same ozone profile but use the ice refractive index the decay is

350   slower and within the range predicted by ozone absorption.

It is important to note that although in the geometry considered here the decay in the observed optical radiation is in most cases dominated by ozone absorption, this is not always be the case as we have seen with the Tropical ozone profile. Once more the key is the interplay between the time scales defined in the previous section and the time scales for ozone absorption in the relevant range of altitudes. For example with a thinner cloud extending only up to 12 km altitude we clearly see the effect

355   of τ_S as defined above.

Table 1. Time-scales defining the photometer response to an impulsive optical source inside a thundercloud.

Symbol	Equation	Description
τ_A	(24)	Absorption by droplets or ice.
τ_D	(28)	Diffusion to the cloud top.
τ_S	(35)	Residence time inside the cloud.
τ_{O3}	(36)	Ozone absorption.

3.3 The time scales involved in photometer waveforms

In the previous sections we introduced four different time scales, summarized in table 1, which affect the photometer response to a lightning flash. Although these timescales have a closed-form expression only within the simplified models that we have considered so far, they nevertheless provide, also in more realistic settings, a useful framework of analysis. But note that a lightning stroke or flash posesses intrinsic timescales left aside in our discussion: the final photometer response results from the convolution of these intrinsic time scales with those introduced by in-cloud scattering.

Our experience leads us to the following broad guidelines for the analysis of photometer pulses:

1. Absorption by ozone molecules (time scale τ_{O3}) is mostly negligible for optical wavelengths but strong below about 300 nm. In the ultra-violet one therefore expects very short pulses, as shown in figure 5.

2. Under most circumstances, absorption by droplet or ice particles (measured by τ_A) is relatively weak and visible only in the tail of the photometer response

3. Usually both the time for diffusion to the cloud-top (τ_D) and the total residence time (τ_S) are relevant, with τ_D affecting mostly the rise-time of the signal and τ_S its decay. This is visible in figure 4, where the rise is captured by an expression that involves only τ_D whereas the decay follows an exponential with characteristic time τ_S.

3.4 Imaging complex geometries

Let us now turn to the imaging capabilities of the CloudScat.jl code combined with complex cloud shapes. As an example we construct the following cloud geometry, that roughly mimics a typical convective thundercloud and is shown in figure 6, panels (a) and (b). Start from a cylindrical base with a radius of 20 km and spanning altitudes between 7 and 10 km above ground. A turret emerges from this base that we model as a vertical truncated cone between altitudes of 10 and 15 km and respective radii of 11.25 km and 7.5 km. The turret is topped by an ellipsoid centered at $(x, y, z) = (0, 0, 15\,\text{km})$ and semi-axes with lengths $(12\,\text{km}, 10\,\text{km}, 2\,\text{km})$. Finally, we dig a hole on the top of the turret by subtracting a 3 km-radius ball centered at $(0, 1\,\text{km}, 17\,\text{km})$. To aid in the visualization of the cloud geometry CloudScat.jl generates code that can be used by the Mathematica software (newer than version 11.2) to render a three-dimensional plot of the cloud shape from a satellite's viewpoint. With this feature we
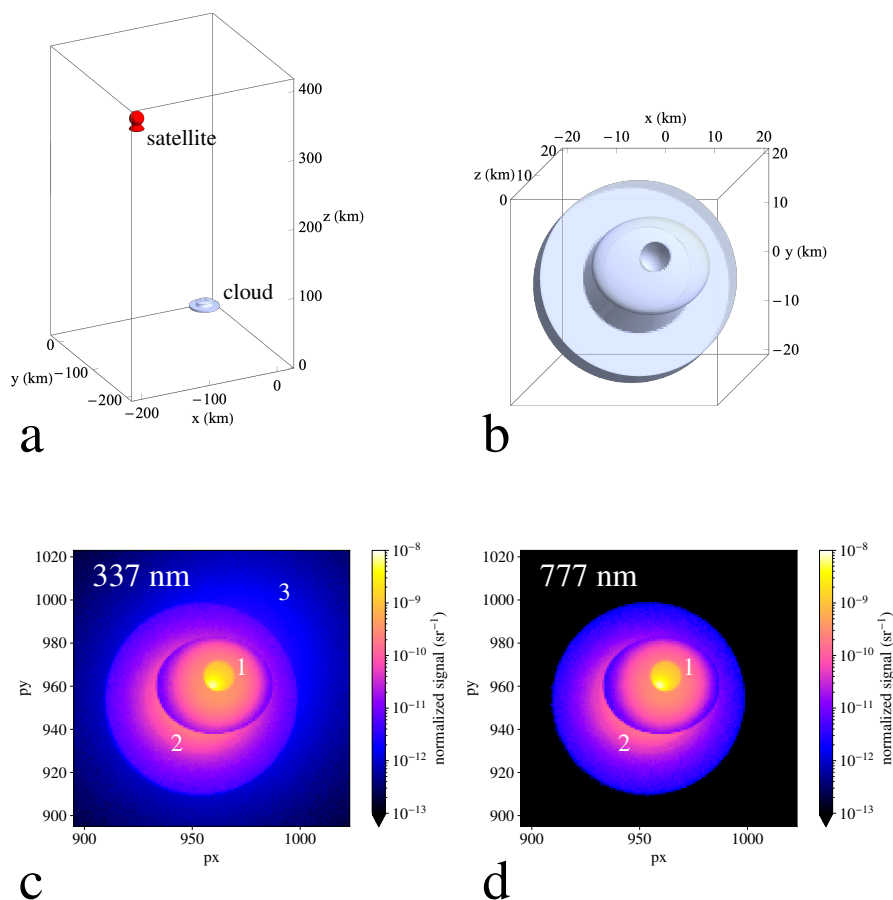
Figure 6. A satellite observes a flash-illuminated complex cloud. The observation geometry is shown in (a), where we represent the cloud geometry and the satellite location. In (b) we show a rendering of the cloud geometry as observed from the satellite's viewpoint. Finally (c) and (d) are the outcome of our Monte Carlo model simulating an image captured by the satellite's camera filtered at 337 nm and 777 nm respectively. In this image we have labelled the hole in the cloud turret (1), the emissions from the lower cloud deck (2) and the surrounding, diffuse Rayleigh emissions (3).

generated panels (a) and (b) in figure 6. The cloud has a homogeneous composition identical to that described in the previous

380 section.

  The figure thus constructed is illuminated by a vertical flash in the z-axis between 8 km and 13 km of altitude and observed by a satellite at coordinates $(-200\,\mathrm{km}, -200\,\mathrm{km}, 400\,\mathrm{km})$. The satellite's camera is modeled after the MMIA cameras: pointing towards the nadir with a field-of-view of 40° (measured as half the diagonal of a square field) an image size of 1024×1024 pixels. We consider the two wavelengths observed by the cameras in MMIA: 337 nm and 777 nm.

385   To predict how this cloud looks like when it is illuminated from the inside by a lightning flash we run our Monte Carlo model with 10^8 photon packets for each of the wavelengths. The result is displayed in panels (c) and (d) of the figure where we

Table 2. Absorption of light of different wavelengths by clouds with droplet radii of 10 and 20 µm and a density 100 cm^{-3}. See the text for the definition of the single-scattering albedo ω_0 and expression (24) for the absorption time.

Wavelength, λ (nm)	Radius, R (µm)	$1 - \omega_0$	Absorption time, τ_A (ms)
337	10	2.8×10^{-6}	18.5
	20	5.6×10^{-6}	2.3
777	10	2.0×10^{-5}	2.5
	20	4.0×10^{-5}	0.3

plot the signal normalized to the number of source photons (i.e. it shows photons in each pixel per stereoradian and per source photon with the considered wavelength).

Remarkably, for both wavelengths the image is dominated by light emanating from the hole (1) at the top (note the logarithmic color scale). This stresses the counter-intuitive features of observing objects illuminated from the inside, as also underlined by Peterson (2019). Quite often the most standing-out features of a lightning flash are depressions in the cloud geometry.

Another feature of both pictures is the illumination of the lower cloud deck (2), partly by light diffusing from inside the cloud, partly by reflection of light emerging from the turret's external boundary. A close look reveals a slight difference between the two wavelengths in the spatial distribution of this brightness, with the 337-nm illumination spreading out somewhat more. This difference will be analyzed in detail in the following section. The darkest areas are those not covered by the cloud, which is also somewhat contrary to our intuition.

One last feature of the simulated image is the weak, diffuse glow away from the brightest areas of the 337-nm picture (3), which is essentially absent in the 777-nm simulation. This glow results from Rayleigh scattering in the atmosphere above and around the cloud. Here these image areas are three to four orders of magnitude dimmer than the brightest features.

3.5 Imaging at different wavelenghts

Our next application is understanding differences in how a lightning source looks as it is imaged at different wavelengths. As we mentioned in the introduction, the MMIA module of ASIM contains cameras with wavelength filters around 337 nm and 777 nm and so we restrict ourselves to these wavelengths.

Solving the Mie scattering problem shows that the extinction parameter (always close to two) and the asymmetry parameter depend only weakly on the radiation wavelength. It is the single-scattering albedo (this is, the absorption by cloud droplets) that dominates the differences between different wavelengths. Table 2 shows the different absorption properties of the cloud microphysical parameters that we have considered in our simulations. Remarkably, the different absorption rates are visible in a cloud-scattered image as a softer, more blurred image in the least absorbed band.

To illustrate this feature we simulate observations of sources within a 20-km-radius cylindrical cloud between 5 and 15 km of altitude (the larger span of the cloud compared with other simulation limits the leakage of photons from the lower edge). The
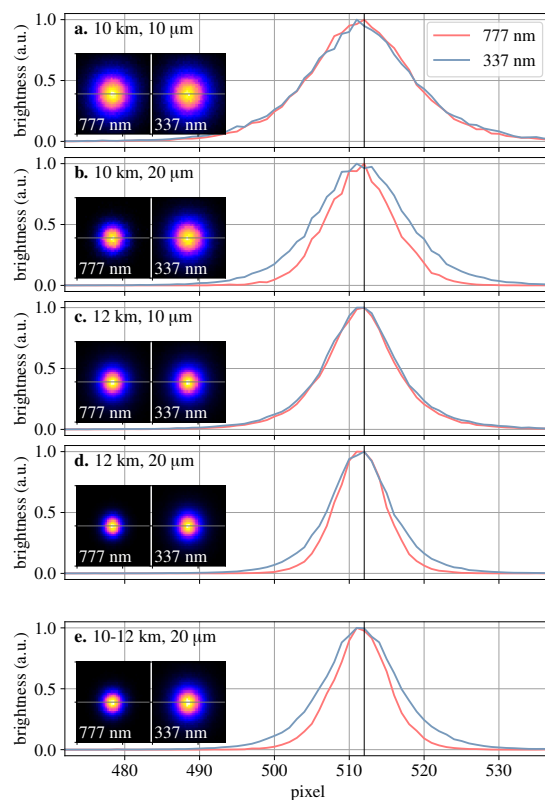
Figure 7. Simulated images of a cloud-scattered source at different wavelengths. Panels (a)-(d) show the integrated radiance produced by a point source at 10 or 12 km within a homogenous cylindrical 20-km-radius cloud spanning altitudes between 5 and 15 km with droplet radius of 10 or 20 μm and droplet concentration of $100\,\mathrm{cm}^{-3}$. Panel (e) shows images of a vertically extended source from 10 to 12 km. All observations are performed in the nadir and in each panel we plot the integrated radiances in a horizontal line crossing the sub-satellite point as well as the full images in each of insets at the left. To ease the comparison, all data and images are normalized to their peak value.

cloud is populated with a droplet density of $100\,\mathrm{cm}^{-3}$ and to emphasize the role of absorption we test droplet radii of 10 and 20 μm, the latter leading to much higher absorption rates. Panels (a)-(d) of figure 7 compare the outcomes of these simulations. We notice that in the two cases most dominated by absorption the emissions of a point source are more spread-out, looking more diffuse. The reason is that photons that travel radially further spend more time inside the cloud and have a higher probability

415 of being absorbed. This reduces the spread of the most-absorbed radiation, which in this case is in the 777 nm-band.

   This effect is somewhat stronger if the light source extends vertically. This is shown in panel (e) of figure 7, which contains results of a simulation similar to those in panels (b) and (d) (i.e. 20-μm droplets) but where the source is a vertical channel with a constant luminosity per unit length extending from 10 to 12 km altitude. We see that in this case the difference between the two wavelengths is even more noticeable than in either of panels (b) or (d). The reason is that, due to a weaker absorption of

420 the 337-nm band, we are capable of see emissions in this wavelength coming from deeper within the cloud and these create a wider image (equation (29) provides a quantitative estimate of this).

3.6 Interpretation of an MMIA observation

As a final application of the code we analyse an actual observation recorded by the MMIA module of ASIM. We chose an event that took place on 22 November 2019 at 08:43:05 at 4.45° N, 77.50° W (about 10 km off the Pacific Coast of Colombia).

425 Panel (a) in figure 8 contains the image from MMIA's 337-nm filtered camera. There is a ring structure that suggests the effect of a cloud turret extending above a lower cloud surface. The cloud turret contains two differentiated regions, the lower being somewhat brighter. Finally, the lower part of the ring surrounding the turret has two maxima to the left and right.

These considerations suggest that the discharge may have taken place below a cloud turret with two lobes and a slight depression in the cloud top to explain the two lower maxima. We therefore constructed the following cloud shape: the cloud

430 base is a 15-km-radius cylinder between 5 and 12 km of altitude. From this cylinder we subtract an ellipsoid with semi-axes $(4\,\mathrm{km}, 6\,\mathrm{km}, 2\,\mathrm{km})$ and centered at $(2\,\mathrm{km}, -4\,\mathrm{km}, 12\,\mathrm{km})$ with respect to the ground point below the base center. The two lobes are represented by ellipsoids, the first one with semi-axes $(4\,\mathrm{km}, 6\,\mathrm{km}, 2\,\mathrm{km})$ and centered at $(-1\,\mathrm{km}, -1\,\mathrm{km}, 12\,\mathrm{km})$ whereas the second has semi-axes $(4\,\mathrm{km}, 5\,\mathrm{km}, 5\,\mathrm{km})$ and is centered at $(-4\,\mathrm{km}, 3\,\mathrm{km}, 12\,\mathrm{km})$. Besides, the dark upper lobe in the MMIA image may indicate a strong absorption at higher altitudes so we imposed an effective droplet radius that grows linearly from

435 $10\,\mu\mathrm{m}$ at the lower boounday of the cloud (5 km) to $20\,\mu\mathrm{m}$ at the upper boundary of the tallest lobe (15 km). The droplet density set to $100\,\mathrm{cm}^{-3}$ everywhere inside the cloud.

The implemented geometry is plotted in panel (c) of figure 8 and the simulation results, in panel (b) can be compared with the direct observation. We made no attempt to rigurously fit the geometry parameters to the observations and, clearly, there are too many possible configurations that would produce similar observations to claim that the hypothesized shape really captures

440 the reality of the cloud. The point of this exercise was rather to show the usefulness of the Monte Carlo model to test hypothesis about the cloud composition and configuration as well as to gain intuition about them.

4 Conclusions

We developed the CloudScat.jl code to assist in the interpretation of space-based observations of lightning-illuminated clouds. We were particularly interested in observations by the MMIA module of the ASIM instrument onboard the International Space

445 Station but we invite the broader research community to experiment with our code and adapt it to other observation platforms.

At present, the cloud microphysics in the code is somewhat oversimplified and does not compete in sophistication with radiative-transport models in other areas of the climate and weather research communities. Future work could address this shortcoming by combining our radiative-transport code with cloud physics models and with additional inputs from other Earth-observing spacecraft. This path, using a different code, has very recently been undertaken by Brunner and Bitzer (2019).

450 Currently the atmospheric electricity community regards the scattering by clouds of lightning-produced optical radiation as a hindrance that prevents a more detailed view of the lightning discharge. But there is another point of view whereby lightning
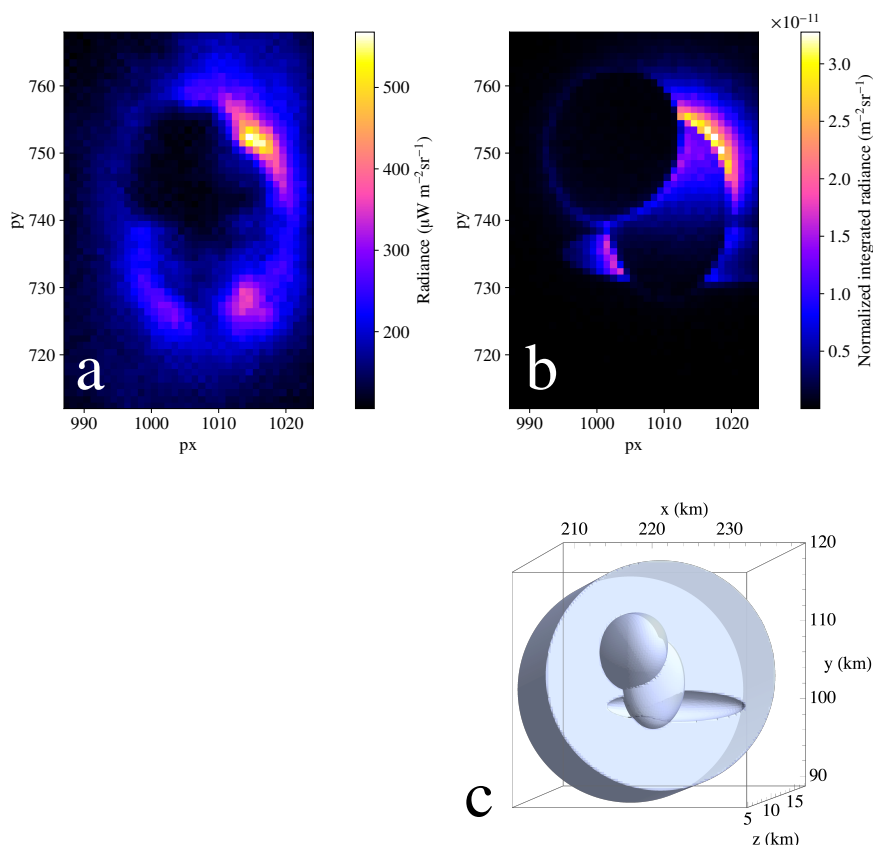
Figure 8. Comparison of a picture from the 337-nm-filtered MMIA camera from ASIM (a) and a simulated observation from our Monte Carlo code (b) with the cloud geometry shown in (c). The MMIA picture was captured by the the 337-nm-filtered camera on 22 November 2019 at 08:43:05 at 4.45° N, 77.50° W.

discharges are beacons that probe the cloud microphysics by allowing a deeper view into them. To realize this possibility one needs, besides good space-borne detectors, reliable numerical codes to interpret the observations. It is our intention that our code serves in this role.

455   *Code availability.* The latest version of our code is available at https://github.com/aluque/CloudScat.jl. For the simulations presented here we used release 1.0rc1 (hash ...), which was archived in a zenodo repository doi:10.5281/zenodo.3842787. As the code is distributed as a julia package the simplest way to install it together with all its dependencies is with the julia package manager by typing "`] add https://github.com/aluque/CloudScat.jl`" at the julia prompt. The repository contains an introduction on the code usage as well as heavily-commented example inputs, including those used to produce the figures of this paper.

Appendix A: Implementation details

The code presented here is implemented in the julia programming language. Although this language is gaining adoption in numerically-intensive research areas, it is still less popular than more established languages such as Python, Fortran and C++. However, we considered it particularly suited for our application because it offers a large amount of flexibility with little or no performance overhead. This is visible in some aspects of our code that we wish to mention.

A significant feature of julia is that each function is compiled at the time of first call with its code being specialized for the given argument types. That means that the compiler uses information contained in these types to optimize the output code.

We make use of this feature in the specification of the cloud composition, where we define different types for homogeneous and inhomogeneous clouds. For an inhomogeneous cloud the code has to call repeatedly a function that probes the cloud composition at each collision location. In principle one could particularize this to a homogeneous cloud by letting this function return always the same value but then we needlessly call this function many times. This is avoided in julia because even if the cloud composition is specified dynamically (i.e. at run time) the subsequent code is specialized depending on whether the cloud is homogeneous or not.

A similar benefit is obtained regarding the cloud geometry, which is defined as a complex structure of nested affine transforms and boolean operations that act on different types of elementary shapes. We encode this structure into a data type and make it available to the compiler. In this case to ensure that the code is fully specialized to the geometry structure we employed another julia feature, which is meta-programming, particularly generated functions. In these functions the code can be constructed dynamically according to the type of the function arguments. We thus dynamically build code tailored to the specific cloud geometry that is then compiled and fully optimized. This ensures the highest possible performance for each configuration.

These kind of optimizations are also available in other compiled languages like Fortran or C++ but in those cases one loses the dynamical capability, leading to a slower development cycle and poorer user experience.

Author contributions. AL designed the study, wrote the numerical code and drafted the manuscript. FJGV, DL, FJPI and AS tested the code and suggested improvements. FJGV, DL, AMR, FJPI, SS, OC, MH, TN and NØ helped in the analysis of ASIM observations. OC, TN, VR and NØ provided access to the ASIM repository and clarified details of MMIA's design. All authors contributed to the final version of the manuscript.

Competing interests. The authors declare that there is no conflict of interest.

Acknowledgements. This work was supported by the European Research Council (ERC) under the European Union H2020 programme/ERC grant agreement 681257. FJGV and SS acknowledge support from the Spanish Ministry of Science and Innovation, MCI under project ESP2017-86263-C4-4-R. FJGV, DL, AMR, SS and AL acknowledge financial support from the State Agency for Research of the Spanish

MCI through the "Center of Excellence Severo Ochoa" award for the Instituto de Astrofísica de Andalucía (SEV-2017-0709). ASIM is a
490   mission of ESA's SciSpace Programme for scientific utilization of the ISS and non-ISS space exploration platforms and space environment
analogues. It is funded by ESA and national contributions through contracts with TERMA and Technical University of Denmark (DTU) in
Denmark, University of Bergen (UB) in Norway and University of Valencia (UV) in Spain.

References

Adachi, T., Sato, M., Ushio, T., Yamazaki, A., Suzuki, M., Kikuchi, M., Takahashi, Y., Inan, U. S., Linscott, I., Hobara, Y., Frey, H. U., Mende, S. B., Chen, A. B., Hsu, R.-R., and Kusunoki, K.: Identifying the occurrence of lightning and transient luminous events by nadir spectrophotometric observation, J. Atm. Sol.-Terr. Phys., 145, 85, https://doi.org/10.1016/j.jastp.2016.04.010, 2016.

Bates, D. R.: Rayleigh scattering by air, Plan. Spac. Sci., 32, 785, https://doi.org/10.1016/0032-0633(84)90102-8, 1984.

Berk, A., Anderson, G. P., Acharya, P. K., Bernstein, L. S., Muratov, L., Lee, J., Fox, M., Adler-Golden, S. M., Chetwynd, J. H., Hoke, M. L., Lockwood, R. B., Gardner, J. A., Cooley, T. W., Borel, C. C., and Lewis, P. E.: MODTRAN 5: a reformulated atmospheric band model with auxiliary species and practical multiple scattering options: update, vol. 5806 of *Society of Photo-Optical Instrumentation Engineers (SPIE) Conference Series*, p. 662, https://doi.org/10.1117/12.606026, 2005.

Blakeslee, R. J.: Non-Quality Controlled Lightning Imaging Sensor (LIS) on International Space Station (ISS) Science Data, https://doi.org/http://dx.doi.org/10.5067/LIS/ISSLIS/DATA107, http://https//ghrc.nsstc.nasa.gov/hydro/details/isslis{_}v1{_}nqc, 2019.

Blakeslee, R. J., Christian, H. J., J., Mach, D. M., Buechler, D. E., Koshak, W. J., Walker, T. D., Bateman, M. G., Stewart, M. F., O'Brien, S., Wilson, T. O., Pavelitz, S. D., and Coker, C.: Lightning Imaging Sensor (LIS) on the International Space Station (ISS): Launch, Installation, Activation, and First Results, in: AGU Fall Meeting Abstracts, vol. 2016, p. AE23A, 2016.

Boccippio, D. J., Koshak, W. J., and Blakeslee, R. J.: Performance Assessment of the Optical Transient Detector and Lightning Imaging Sensor. Part I: Predicted Diurnal Variability, Journal of Atmospheric and Oceanic Technology, 19, 1318, https://doi.org/10.1175/1520-0426(2002)019<1318:PAOTOT>2.0.CO;2, 2002.

Bodhaine, B. A., Wood, N. B., Dutton, E. G., and Slusser, J. R.: On Rayleigh Optical Depth Calculations, Journal of Atmospheric and Oceanic Technology, 16, 1854, https://doi.org/10.1175/1520-0426(1999)016<1854:ORODC>2.0.CO;2, 1999.

Bohren, C. and Huffman, D. R.: Absorption and Scattering of Light by Small Particles, John Wiley & Sons, New York, USA, 1983.

Bozem, H., Fischer, H., Gurk, C., Schiller, C. L., Parchatka, U., Koenigstedt, R., Stickler, A., Martinez, M., Harder, H., Kubistin, D., Williams, J., Eerdekens, G., and Lelieveld, J.: Influence of corona discharge on the ozone budget in the tropical free troposphere: a case study of deep convection during GABRIEL, Atmospheric Chemistry & Physics, 14, 8917, https://doi.org/10.5194/acp-14-8917-2014, 2014.

Brunner, K. N. and Bitzer, P. M.: A first look at cloud inhomogeneity and its effect on lightning optical emission, Geophysical Research Letters, n/a, e2020GL087 094, https://doi.org/10.1029/2020GL087094, https://agupubs.onlinelibrary.wiley.com/doi/abs/10.1029/2020GL087094, 2019.

Cecil, D. J., Buechler, D. E., and Blakeslee, R. J.: Gridded lightning climatology from TRMM-LIS and OTD: Dataset description, Atmospheric Research, 135, 404, https://doi.org/10.1016/j.atmosres.2012.06.028, 2014.

Chanrion, O., Neubert, T., Mogensen, A., Yair, Y., Stendel, M., Singh, R., and Siingh, D.: Profuse activity of blue electrical discharges at the tops of thunderstorms, Geophys. Res. Lett., 44, 496, https://doi.org/10.1002/2016GL071311, 2017.

Chanrion, O., Neubert, T., Lundgaard Rasmussen, I., Stoltze, C., Tcherniak, D., Jessen, N. C., Polny, J., Brauer, P., Balling, J. E., Savstrup Kristensen, S., Forchhammer, S., Hofmeyer, P., Davidsen, P., Mikkelsen, O., Bo Hansen, D., Bhanderi, D. D. V., Petersen, C. G., and Lorenzen, M.: The Modular Multispectral Imaging Array (MMIA) of the ASIM Payload on the International Space Station, Space Sci. Rev., 215, 28, https://doi.org/10.1007/s11214-019-0593-y, 2019.

Chern, J. L., Hsu, R. R., Su, H. T., Mende, S. B., Fukunishi, H., Takahashi, Y., and Lee, L. C.: Global survey of upper atmospheric transient luminous events on the ROCSAT-2 satellite, J. Atm. Sol.-Terr. Phys., 65, 647, https://doi.org/10.1016/S1364-6826(02)00317-6, 2003.

530   Christian, H. J., Blakeslee, R. J., Boccippio, D. J., Boeck, W. L., Buechler, D. E., Driscoll, K. T., Goodman, S. J., Hall, J. M., Koshak, W. J., Mach, D. M., and Stewart, M. F.: Global frequency and distribution of lightning as observed from space by the Optical Transient Detector, J. Geophys. Res. (Atmos.), 108, 4005, https://doi.org/10.1029/2002JD002347, 2003.

Dwyer, J. R., Smith, D. M., and Cummer, S. A.: High-Energy Atmospheric Physics: Terrestrial Gamma-Ray Flashes and Related Phenomena, Space Sci. Rev., 173, 133, https://doi.org/10.1007/s11214-012-9894-0, 2012.

535   Ebert, U., Nijdam, S., Li, C., Luque, A., Briels, T., and van Veldhuizen, E.: Review of recent results on streamer discharges and discussion of their relevance for sprites and lightning, J. Geophys. Res. (Space Phys), 115, A00E43, https://doi.org/10.1029/2009JA014867, 2010.

Goodman, S. J., Blakeslee, R. J., Koshak, W. J., Mach, D., Bailey, J., Buechler, D., Carey, L., Schultz, C., Bateman, M., McCaul, E., and Stano, G.: The GOES-R Geostationary Lightning Mapper (GLM), Atmospheric Research, 125, 34, https://doi.org/10.1016/j.atmosres.2013.01.006, 2013.

540   Hale, G. M. and Querry, M. R.: Optical constants of water in the 200-nm to 200-micrometer wavelength region, App. Opt., 12, 555, https://doi.org/10.1364/AO.12.000555, 1973.

Haynes, W.: CRC Handbook of Chemistry and Physics, 97th edition, CRC Press, https://books.google.es/books?id=VVezDAAAQBAJ, 2016.

Iwabuchi, H.: Efficient Monte Carlo Methods for Radiative Transfer Modeling, Journal of Atmospheric Sciences, 63, 2324, https://doi.org/10.1175/JAS3755.1, 2006.

545   Kneizys, F. X., Shettle, E. P., Gallery, W. O., Chetwynd, J. H., J., Abreu, L. W., McClatchey, R. A., Fenn, R. W., and Selby, J. E. A.: Atmospheric transmittance/radiance: Computer code LOWTRAN 5, Unknow, 1980.

Koshak, W. J., Solakiewicz, R. J., Phanord, D. D., and Blakeslee, R. J.: Diffusion model for lightning radiative transfer, J. Geophys. Res., 99, 14,361–14,371, https://doi.org/10.1029/94JD00022, 1994.

Krapivsky, P., Redner, S., and Ben-Naim, E.: A Kinetic View of Statistical Physics, Cambridge University Press, 2010.

550   Le Vine, D. M.: Sources of the strongest RF radiation from lightning, J. Geophys. Res., 85, 4091, https://doi.org/10.1029/JC085iC07p04091, 1980.

Light, T. E., Suszcynsky, D. M., Kirkland, M. W., and Jacobson, A. R.: Simulations of lightning optical waveforms as seen through clouds by satellites, J. Geophys. Res., 106, 17,103–17,114, https://doi.org/10.1029/2001JD900051, 2001.

Liu, F., Zhu, B., Lu, G., Qin, Z., Lei, J., Peng, K.-M., Chen, A. B., Huang, A., Cummer, S. A., Chen, M., Ma, M., Lyu, F., and Zhou, H.:
555   Observations of Blue Discharges Associated With Negative Narrow Bipolar Events in Active Deep Convection, Geophys. Res. Lett., 45, 2842, https://doi.org/10.1002/2017GL076207, 2018.

Mach, D. M., Christian, H. J., Blakeslee, R. J., Boccippio, D. J., Goodman, S. J., and Boeck, W. L.: Performance assessment of the Optical Transient Detector and Lightning Imaging Sensor, J. Geophys. Res. (Atmos.), 112, D09210, https://doi.org/10.1029/2006JD007787, 2007.

Minschwaner, K., Anderson, G. P., Hall, L. A., and Yoshino, K.: Polynomial coefficients for calculating O_2 Schumann-Runge cross sections
560   at 0.5 cm^{-1} resolution, J. Geophys. Res., 97, 10 103, https://doi.org/10.1029/92JD00661, 1992.

Molina, L. T. and Molina, M. J.: Absolute absorption cross sections of ozone in the 185- to 350-nm wavelength range, J. Geophys. Res., 91, 14 501, https://doi.org/10.1029/JD091iD13p14501, 1986.

Neubert, T., Østgaard, N., Reglero, V., Chanrion, O., Heumesser, M., Dimitriadou, K., Christiansen, F., Budtz-Jorgensen, C., Kuvvetli, I., Rasmussen, I. L., Mezentsev, A., Marisaldi, M., Ullaland, K., Genov, G., Yang, S., Kochkin, P., Navarro-Gonzalez, J., Connell,
565   P. H., and Eyles, C. J.: A terrestrial gamma-ray flash and ionospheric ultraviolet emissions powered by lightning, Science, 367, 183, https://doi.org/10.1126/science.aax3872, 2020.

Pan, L. L., Homeyer, C. R., Honomichl, S., Ridley, B. A., Weisman, M., Barth, M. C., Hair, J. W., Fenn, M. A., Butler, C., Diskin, G. S., Crawford, J. H., Ryerson, T. B., Pollack, I., Peischl, J., and Huntrieser, H.: Thunderstorms enhance tropospheric ozone by wrapping and shedding stratospheric air, Geophys. Res. Lett., 41, 7785, https://doi.org/10.1002/2014GL061921, 2014.

Pasko, V. P., Yair, Y., and Kuo, C.-L.: Lightning Related Transient Luminous Events at High Altitude in the Earth's Atmosphere: Phenomenology, Mechanisms and Effects, Space Sci. Rev., 168, 475, https://doi.org/10.1007/s11214-011-9813-9, 2012.

Peck, E. R. and Reeder, K.: Dispersion of Air, Journal of the Optical Society of America (1917-1983), 62, 958, 1972.

Peterson, M.: Using Lightning Flashes to Image Thunderclouds, J. Geophys. Res. (Atmos.), 124, 10,175–10,185, https://doi.org/10.1029/2019JD031055, 2019.

Peterson, M. and Rudlosky, S.: The Time Evolution of Optical Lightning Flashes, J. Geophys. Res. (Atmos.), 124, 333, https://doi.org/10.1029/2018JD028741, 2019.

Rison, W., Krehbiel, P. R., Stock, M. G., Edens, H. E., Shao, X.-M., Thomas, R. J., Stanley, M. A., and Zhang, Y.: Observations of narrow bipolar events reveal how lightning is initiated in thunderstorms, Nature Communications, 7, 10721, https://doi.org/10.1038/ncomms10721, 2016.

Sato, M., Takahashi, Y., Kikuchi, M., Suzuki, M., Yamazaki, A., and Ushio, T.: Lightning and Sprite Imager (LSI) Onboard JEM-GLIMS, IEEJ Transactions on Fundamentals and Materials, 131, 994, https://doi.org/10.1541/ieejfms.131.994, 2011.

Smith, D. A., Shao, X. M., Holden, D. N., Rhodes, C. T., Brook, M., Krehbiel, P. R., Stanley, M., Rison, W., and Thomas, R. J.: A distinct class of isolated intracloud lightning discharges and their associated radio emissions, J. Geophys. Res., 104, 4189, https://doi.org/10.1029/1998JD200045, 1999.

Soler, S., Pérez-Invernón, F. J., Gordillo-Vázquez, F. J., Luque, A., Li, D., Malagón-Romero, A., Neubert, T., Chanrion, O., Reglero, V., Navarro-González, J., Lu, G., Zhang, H., Huang, A., and Østgaard, N.: Blue optical observations of narrow bipolar events by ASIM confirm corona streamer activity in thunderstorms, J. Geophys. Res. (Atmos.) (submitted), 2020.

Thomason, L. W. and Krider, E. P.: The Effects of Clouds on the Light Produced by Lightning., Journal of Atmospheric Sciences, 39, 2051, https://doi.org/10.1175/1520-0469(1982)039<2051:TEOCOT>2.0.CO;2, 1982.

Tilles, J. N., Liu, N., Stanley, M. A., Krehbiel, P. R., Rison, W., Stock, M. G., Dwyer, J. R., Brown, R., and Wilson, J.: Fast negative breakdown in thunderstorms, Nature Communications, 10, 1648, https://doi.org/10.1038/s41467-019-09621-z, 2019.

United States Committee on Extension to the Standard Atmosphere: U.S. standard atmosphere, 1976, National Oceanic and Amospheric [sic] Administration : for sale by the Supt. of Docs., U.S. Govt. Print. Off., 1976.

van de Hulst, H.: Light Scattering by Small Particles, Dover Books on Physics, Dover Publications, 1981.

Warren, S. G. and Brandt, R. E.: Optical constants of ice from the ultraviolet to the microwave: A revised compilation, J. Geophys. Res. (Atmos.), 113, D14220, https://doi.org/10.1029/2007JD009744, 2008.

Wilkman, O.: MieScatter, https://github.com/dronir/MieScatter.jl, 2013.

Zhang, D., Cummins, K. L., Bitzer, P., and Koshak, W. J.: Evaluation of the Performance Characteristics of the Lightning Imaging Sensor, Journal of Atmospheric and Oceanic Technology, 36, 1015, https://doi.org/10.1175/JTECH-D-18-0173.1, 2019.